INTERNATIONAL JOURNAL FOR NUMERICAL METHODS IN FLUIDS
Int. J. Numer. Meth. Fluids 2002; **40**:875–901 (DOI: 10.1002/fld.380)

Injection/suction boundary conditions for fluid–structure interaction simulations in incompressible flow

G. Medic[1,*,†] and B. Mohammadi[2,‡]

[1]*Flow Physics and Computation Division, Mechanical Engineering Department, Stanford University, Stanford, CA 95304-3030, U.S.A.*
[2]*INRIA Rocquencourt, Project M3N, 78153 Le Chesnay, France*

SUMMARY

This paper presents the analysis of injection/suction boundary conditions in the context of the fluid–structure interactions simulation of the incompressible turbulent flow.

First, the equations used in the modelling of the fluid and the structure are presented, as well as the numerical methods used in the corresponding solvers. Injection/suction boundary conditions are then presented with details of different implementation alternatives. Arbitrary Lagrangian–Eulerian (ALE) approach was also implemented in order to test the injection/suction boundary conditions.

Numerical tests are performed where injection/suction boundary conditions are compared to ALE simulations. These tests include forced movement of the structure and two-degrees-of-freedom structure model simulations. Copyright © 2002 John Wiley & Sons, Ltd.

KEY WORDS: injection/suction conditions; fluid–structure interactions; incompressible turbulent flow

1. INTRODUCTION

In this analysis of fluid–structure interaction problems we investigated the possibility of the application of injection/suction boundary conditions in the context of the stability analysis of civil engineering constructions (see, for example, References [1–4]). When applying injection/suction boundary conditions in a fluid–structure interactions simulation, the effects of the cross-section movements are taken into account in the flow solver by a change in the boundary conditions (see References [5–7]) in order to avoid more costly arbitrary Lagrangian–Eulerian (ALE) formulations (see References [8–15]). Different implementations of injection/suction boundary conditions were already tested in the aeroelastic simulations of compressible flows over airfoils (see References [16–19]), including shape optimization and optimal control applications.

* Correspondence to: G. Medic, Flow Physics and Computation Division, Mechanical Engineering Department, Stanford University, Stanford, CA 95304-3030, U.S.A.
† E-mail: gmedic@stanford.edu
‡ E-mail: Bijan.Mohammadi@inria.fr

Received 5 October 2000
Revised 29 March 2002

In civil engineering applications, we are usually dealing with incompressible turbulent flows. We opted to use Reynolds-averaged Navier–Stokes (RANS) equations together with simple turbulence models, such as k–ε model with the application of wall-laws [20, 21]. There has been some discussion References [22–25] whether RANS equations approach can be applied to unsteady flows (partly based on the insistence that Reynolds averaging equals temporal averaging—which is not), where it was proposed that there should be a spectral gap between the unsteadiness and the turbulence. A more correct criterion for statistical periodicity is that the frequency spectrum should contain a very narrow spike(s), at a shedding frequency(ies), representing the mean unsteadiness (see Reference [25]). In the same way, the simulation of fluid–structure interactions might be carried out using RANS approach as long as there are some distinct oscillations frequencies (large-scale unsteadiness).

The numerical solver NSIKE (see Reference [26]) is based on P1/P1 finite element method for the velocity/pressure pair of variables (U–P) and a P1 discretization for the turbulence variables (k and ε). Chorin's non-incremental projection method is used to decouple the velocity and pressure computation (see References [27, 28]). The time discretization is fully explicit, with Petrov–Galerkin formulation for the intermediate velocity and turbulent variables computation. The convective part of the equations is solved using a positive streamwise invariant (PSI) residual distributions scheme [29] and the viscous term is discretized using the standard Galerkin technique. The pressure equation is solved using a preconditioned conjugate gradient algorithm.

At first, we tested our unstructured solver for various unsteady turbulent incompressible flows over a typical viaduct cross-sections (see References [30, 31]) for which experimental data were available. The results are compared with available experiments.

Variants of injection/suction boundary conditions are then derived and implemented in our original incompressible solver that had to be adapted. In order to evaluate the behaviour of injection/suction boundary conditions we decided to implement the ALE formulation in the solver. In that way, we could compare the two approaches within the same solver.

Simple tests were performed to evaluate the behaviour of injection/suction boundary conditions (see also Reference [31]). The first test concerned the analysis of attached steady incompressible turbulent flow over a well-profiled body such as a NACA profile inclined for a small angle (where the displacement was taken into account by injection/suction boundary conditions). The second test consisted in imposing a periodic movement to the same profile (small amplitude rotational oscillations), and comparing the results of simulations using injection/suction boundary conditions to ALE simulations. And finally, we repeated the first test for the injection/suction boundary conditions for the flow over a rectangle profile (in this case, in an unsteady flow). The results from these tests obtained with different injection/suction boundary conditions are compared and analysed.

After the preliminary tests, we proceeded with the application of our approach in the stability analysis of rectangle profile.

Usually, the first step in aeroelastic investigation is the response of the structure to a forced perturbation. In this approach no dynamic model is used and a periodic movement is prescribed for the cross-section (e.g. in a form of torsional oscillations). The hysteresis curves are used to predict the response of the coupled system by means of engineering criteria. Numerical results for the rectangle profile are compared to the experimental results available in the literature (see References [1–4]).

Finally, we use a rigid body dynamics model based on two ordinary differential equations for torsional and vertical displacement of the cross-section. This model uses at each instant the lift and drag forces produced by the flow and encapsulates the main structure mechanical characteristics. Numerical simulations are carried out for the rectangle profile both with injection/suction boundary conditions and using ALE formulation and the results are analysed using the experimental results from the stability analysis in forced movement ([1–3]). We are interested in the consistency of these results with the ones from the forced movement analysis.

2. UNSTEADY TURBULENT FLOW COMPUTATIONS

Our unsteady turbulent flow computations are based on solving the incompressible Reynolds averaged Navier–Stokes equations with the k–ε model in Ω:

$$\nabla \cdot U = 0 \tag{1}$$

$$\partial_t U + U \cdot \nabla U + \nabla P/\rho - \nabla \cdot ((\nu + \nu_t)(\nabla U + \nabla U^{\mathrm{T}})) = 0 \tag{2}$$

$$\partial_t k + U \cdot \nabla k - \nabla \cdot ((\nu + \nu_t)\nabla k) = S_k \tag{3}$$

$$\partial_t \varepsilon + U \cdot \nabla \varepsilon - \nabla \cdot ((\nu + c_\varepsilon \nu_t)\nabla \varepsilon) = S_\varepsilon \tag{4}$$

with $S_k = \frac{1}{2}\nu_t|\nabla U + \nabla U^t|^2 - \varepsilon$ and $S_\varepsilon = \frac{1}{2}c_1 k|\nabla U + \nabla U^t|^2 - c_2\varepsilon^2/k$ and $\nu_t = c_\mu k^2/\varepsilon$, where U, P, ρ, k, ε, ν and ν_t are, respectively, the mean velocity vector, mean pressure, density, kinetic energy of turbulence, turbulent dissipation, kinematic viscosity and turbulent viscosity. The constants values we use, $c_\mu = 0.09$, $c_1 = 0.1296$, $c_2 = 11/6$ and $c_\varepsilon = 1/1.4245$, are slightly different from those proposed originally by Launder (these values agree better with experimental data for the decay of homogeneous turbulence, for more details see the discussion in Reference [30]). Furthermore, we do not take into account the turbulent contributions in the pressure.

Typically, the boundary of the flow domain Ω is divided into three parts $\partial\Omega = \Gamma_1 \cup \Gamma_2 \cup \Gamma_3$ where Γ_1 represents the inflow boundary (with given U, k and ε), Γ_2 the outflow boundary (no tractions, $\partial k/\partial n = 0$ and $\partial\varepsilon/\partial n = 0$) and Γ_3 represents the solid wall where we impose the wall-laws.

We define the new fictitious boundary Γ_δ in the vicinity of the part of the boundary $\partial\Omega$ that corresponds to the solid wall (Figure 1).

In other words, we transform our original domain Ω in $\Omega_\delta = \Omega - B_\delta$ with

$$B_\delta = \{x - n(x)\lambda : x \in \Gamma_w, \lambda \in (0, \delta(x))\} \tag{5}$$

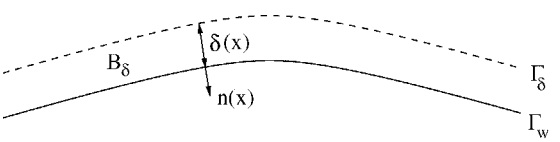

Figure 1. Wall-laws definition.

where usually we take for $\delta(x)$ a constant value for all the solid boundary (or piecewise constant). Then we apply on Γ_δ:

$$U \cdot n = 0, \qquad (S \cdot n \cdot s)s = -u_\tau^2 s \tag{6}$$

$$k = \frac{u_\tau^2}{\sqrt{c_\mu}}\,\alpha, \qquad \varepsilon = \frac{u_\tau^3}{\kappa\delta}\,\min(1, \alpha + 0.3(1-\alpha)^2) \tag{7}$$

where $S = (\nu + \nu_t)(\nabla U + \nabla U^{\mathrm{T}})$, $\kappa = 0.41$, $\alpha = \min(1, y^+/10)$ with $y^+ = u_\tau \delta/\nu$, and $s = (U - (U \cdot n)n)/|U - (U \cdot n)n|$. The friction velocity u_τ is computed using Reichardt wall function

$$\frac{U \cdot s}{u_\tau} = 2.5 \ln(1 + \kappa y^+) + 7.8 \left(1 - \mathrm{e}^{-y^+/11} - \frac{y^+}{11}\,\mathrm{e}^{-0.33 y^+}\right) \tag{8}$$

2.1. Flow solver

Our incompressible solver NSIKE [26] is based on Chorin's projection method for Navier–Stokes equations (see References [27, 28]). We use finite element discretization coupled with residual distribution techniques [29] (written as Petrov–Galerkin finite element schemes), based on P1/P1 elements for the pair of variables velocity/pressure, together with P1 elements for turbulent variables. The computation of intermediate velocity $\tilde{U}$, k and ε is completely explicit, while the pressure problem is solved using preconditioned conjugate gradient technique.

Step 1: *Intermediate velocity and turbulence variables computation*
Let

$$V_h = \{\psi_h : \Omega_h \to R, \psi_h \in C^0(\Omega_h) : \forall K_j \in \Omega_h, \psi_h|_{K_j} \in P^1\} \tag{9}$$

$$J_{0nh} = \{\phi_h \in V_h^d, \phi_h = 0 \text{ on } \Gamma_{1h}, \phi_h \cdot n_h = 0 \text{ on } \Gamma_{3h}\} \tag{10}$$

$$W_{0h} = \{w_h \in V_h, w_h = 0 \text{ on } \Gamma_{1h} \cup \Gamma_{3h}\} \tag{11}$$

Introducing fully explicit time discretization we can write the following Petrov–Galerkin formulation for the intermediate velocity and turbulent variables:

Find $\tilde{U}_h^{n+1}$ such that, $\forall \phi_h \in J_{0nh}$

$$\left(\frac{\tilde{U}_h^{n+1} - U_h^n}{T}, \phi_h\right) + (U_h^n \cdot \nabla U_h^n, \phi_h) + (S_h^n, \nabla \phi_h) - \int_{\Gamma_{3h}} S_h^n \cdot n \cdot \phi_h$$
$$+ \sum_{K, K \in \Omega_h} \int_K \left(\frac{\tilde{U}_h^{n+1} - U_h^n}{T} + U_h^n \cdot \nabla U_h^n - \nabla \cdot S_h^n\right) \cdot g_1^K(V_h^n, \phi_h) = 0 \tag{12}$$

$$\tilde{U}_h^{n+1} - v_h' \in J_{0nh} \tag{13}$$

where v_h' is an approximation of v' in V_h^d, and v' is an extension of v in $H^1(\Omega)^d$ satisfying $v \cdot n = 0$ on Γ_3, v being the function defining Dirichlet boundary conditions on Γ_1 (we also use the usual notation (a, b) for the scalar product).

Find $k_h^{n+1}, \varepsilon_h^{n+1}$ such that, $\forall w_h \in W_{0h}$

$$\left(\frac{k_h^{n+1}-k_h^n}{T}, w_h\right) + (U_h^n \cdot \nabla k_h^n, w_h) + \left(c_\mu \frac{(k_h^n)^2}{\varepsilon_h^n} \nabla k_h^n, \nabla w_h\right) - (S_{k\,h}^n, w_h)$$
$$+ \sum_{K, K \in \Omega_h} \int_K \left(\frac{k_h^{n+1}-k_h^n}{T} + U_h^n \cdot \nabla k_h^n - \nabla \cdot \left(c_\mu \frac{(k_h^n)^2}{\varepsilon_h^n} \nabla k_h^n\right) - S_{k\,h}^n\right) g_2^K(U_h^n, k_h^n, w_h) = 0 \tag{14}$$

$$\left(\frac{\varepsilon_h^{n+1}-\varepsilon_h^n}{T}, w_h\right) + (U_h^n \cdot \nabla \varepsilon_h^n, w_h) + \left(c_\varepsilon \frac{(k_h^n)^2}{\varepsilon_h^n} \nabla \varepsilon_h^n, \nabla w_h\right) - (S_{\varepsilon\,h}^n, w_h)$$
$$+ \sum_{K, K \in \Omega_h} \int_K \left(\frac{\varepsilon_h^{n+1}-\varepsilon_h^n}{T} + U_h^n \cdot \nabla \varepsilon_h^n - \nabla \cdot \left(c_\varepsilon \frac{(k_h^n)^2}{\varepsilon_h^n} \nabla \varepsilon_h^n\right) - S_{\varepsilon\,h}^n\right) g_2^K(U_h^n, \varepsilon_h^n, w_h) = 0 \tag{15}$$

$$k_h^{n+1} - k_h' \in W_{0h}, \qquad \varepsilon_h^{n+1} - \varepsilon_h' \in W_{0h} \tag{16}$$

where k_h' and ε_h' are the approximations of functions k' and ε' in V_h, where k' and ε' are the functions in $H^1(\Omega)$ that satisfy $k' = k_\Gamma$ on Γ_1, $k' = k_w$ on Γ_3, and $\varepsilon' = \varepsilon_\Gamma$ on Γ_1, $\varepsilon' = \varepsilon_w$ on Γ_3, respectively.

Let $\{\psi_i\}_{1,\ldots,N}$ be the basis of $V_{0h} = \{\psi_h \in V_h, \psi_h = 0 \text{ on } \Gamma_{1h}\}$, and let $\{\phi_{i,j}\}_{1,\ldots,N, j=1,\ldots,d}$ be the basis of J_{0nh} defined as

$$\phi_{i,1} = n_i \psi_i, \qquad \phi_{i,2} = s_i^1 \psi_i, \qquad \phi_{i,3} = s_i^2 \psi_i, \quad \text{if } q^i \in \Gamma_{3h} \tag{17}$$

$$\phi_{i,j} = \psi_{i,j} e_j, \qquad j = 1, \ldots, d \quad \text{elsewhere} \tag{18}$$

with $s = s^1 + s^2$, s being the unit tangent defined before, and $\{n, s^1, s^2\}$ being the local orthonormal co-ordinate system with positive orientation, defined for each node q^i and $\{e_j\}$ represent the canonical basis of R^d. Let $\{\psi_i\}_{1,\ldots,N}$ be the basis of W_{0h}.

For determining the system of equations for the computation of nodal values $\tilde{U}_{i,j}^{n+1}$, k_i^{n+1} and ε_i^{n+1} we take the above basis functions as ϕ_h and w_h in (12)–(16). We will not apply the stabilization on the non-stationary term, and that will together with mass lumping (the Gaussian points of numerical integration coincide with the element nodes) while integrating non-stationary term lead to the decoupling of the discrete equations for $\tilde{U}_{i,j}^{n+1}$, k_i^{n+1} and ε_i^{n+1}. Functions defining the stabilization are chosen as $g_1^K = \beta^K(U_h^n, \phi_h) - \phi_h$, $g_2^K = \beta^K(U_h^n, k_n^h, w_h) - w_h$ and $g_2^K = \beta^K(U_h^n, \varepsilon_n^h, w_h) - w_h$, with β^K given by PSI residual distribution scheme [29].

Step 2: *Pressure computation*

Let

$$Q_{0h} = \{\psi_h \in V_h, \psi_h = 0 \text{ on } \Gamma_{2h}\} \tag{19}$$

The Galerkin finite element formulation of the Poisson problem for φ is: Find $\varphi_h^{n+1} \in Q_{0h}$ such that, $\forall \psi_h \in Q_{0h}$

$$\int_{\Omega_h} \nabla \varphi_h^{n+1} \cdot \nabla \psi_h = -\int_{\Omega_h} \nabla \cdot \tilde{U}_h^{n+1} \psi_h \tag{20}$$

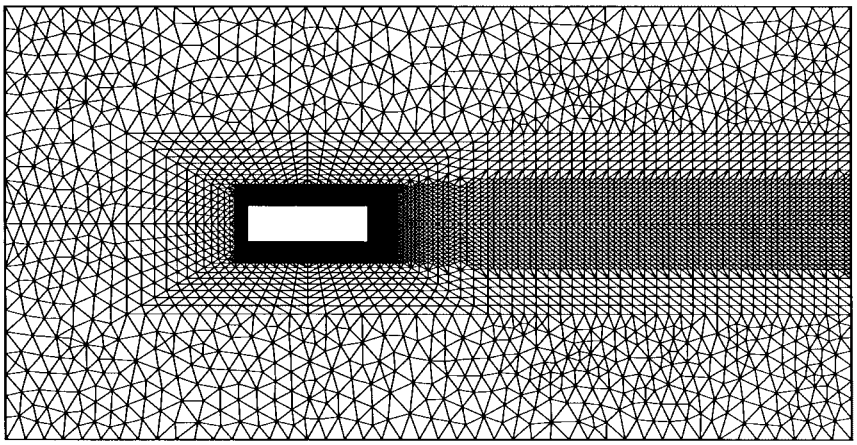

Figure 2. Rectangle profile, $Re_d = 20\,000$, computational mesh, 5412 nodes, 10 426 elements.

Let $\{\psi_i\}_{1,\ldots,N}$ be the basis of Q_{0h}. Taking these basis functions as ψ_h in previous formulation, together with Dirichlet boundary conditions and the introduction of the finite element discretization leads to the linear system solved using preconditioned conjugate gradient method.

Step 3: *Velocity update*
Find V_h^{n+1} such that, $\forall \phi_h \in J_{0nh}$

$$(V_h^{n+1}, \phi_h) = (\tilde{U}_h^n, \phi_h) - (\nabla \varphi_h^{n+1}, \phi_h) \tag{21}$$

$$\tilde{U}_h^{n+1} - v_h' \in J_{0nh} \tag{22}$$

where v_h' is an approximation of v' in V_h^d, and v' is an extension of v in $H^1(\Omega)^d$ satisfying $v \cdot n = 0$ on Γ_3.

2.2. Numerical results for rectangle profile

Our flow solver has been tested for several unsteady flows over cylinders of different cross-section (see also References [30, 26]).

In this analysis, turbulent flow over a simplified viaduct cross-section, i.e. a rectangular with width/height ratio $c/d = 4$, is computed. Computations have been carried out for $Re_d = u_\infty d/v = 20\,000$, using the mesh with ~ 5400 nodes (see Figure 2). In the wall-laws we used $\delta = 0.005c$ giving y^+ values around 20.

This flow is more complex than the flow over a square cylinder, and the recirculation zone behind the cylinder is more difficult to predict correctly (see Figure 3).

The periods of the oscillation of lift and drag forces (and the moment around the profile center of gravity) are described by the corresponding Strouhal numbers: $St_D = f_D d/u_\infty = 0.26$ and $St_L = f_L d/u_\infty = 0.13$ (see Figure 4). These computational values agree very well with the experimental values given in Reference [1]. Furthermore, computed values of drag and lift

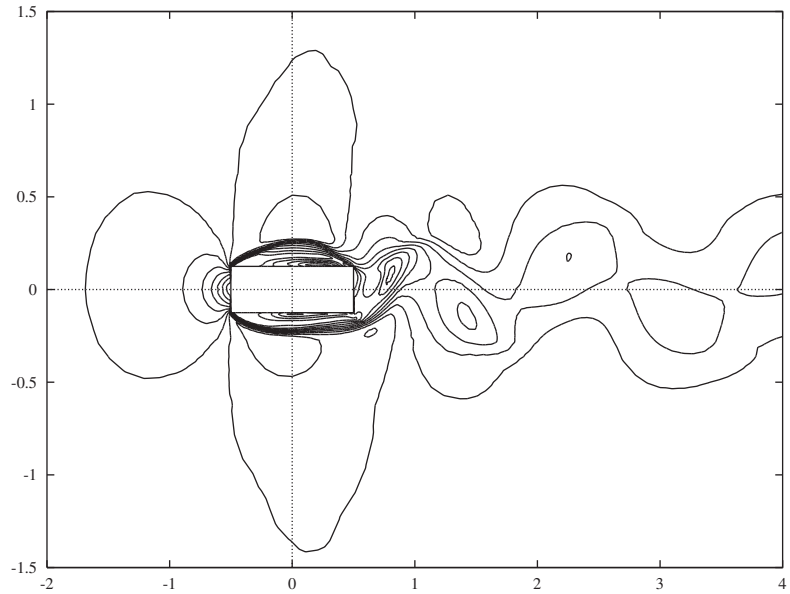

Figure 3. Rectangle profile, $Re_d = 20\,000$, instantaneous iso-$|u|$ contours.

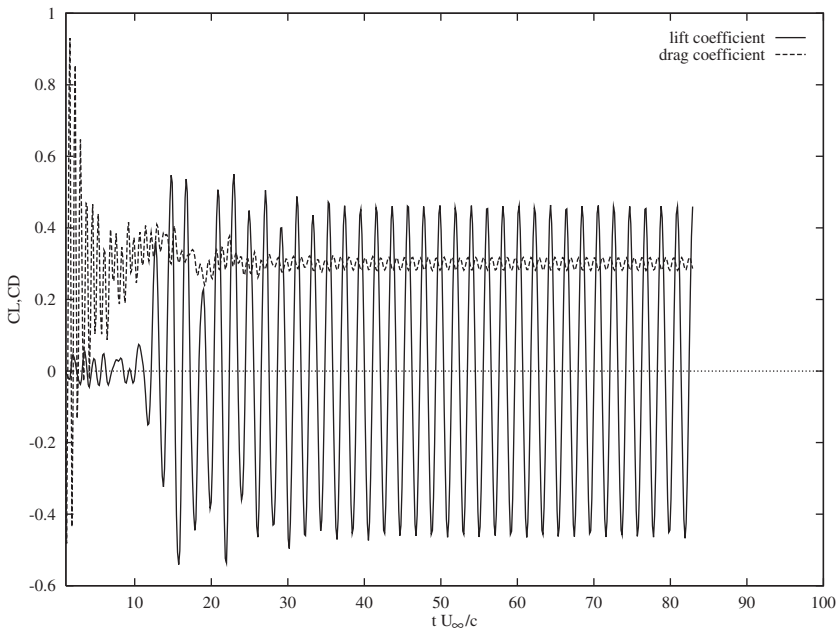

Figure 4. Rectangle profile, $Re_d = 20\,000$, C_{D} and C_{L} coefficients history.

coefficients also agree very well with the experimental values: computed time-averaged drag coefficient $\bar{c}_D = 0.29$ vs experimental time-averaged drag coefficient $\bar{c}_{D,\exp} \sim 0.3$.

3. DOMAINS WITH MOVING BOUNDARIES

In this section, we describe the ingredients used to simulate the boundary movement by means of both the injection/suction boundary conditions [31, 16, 18, 19], and ALE formulation (dynamic mesh method) [8–15, 32].

The problem consists in solving the Navier–Stokes equation in a domain $\Omega_F^m(t)$ that changes in time. In particular, when treating fluid–structure interaction problems, it is usually the structure that changes its position (and shape) in time $\Omega_S^m(t)$ and as a consequence the interface between the fluid domain Ω_F and the structure domain Ω_S is also time dependent $\Gamma_{F/S}^m(t)$. Here, we will be interested in two types of problems. First we will impose a given periodic movement to the structure, and later we will associate a simple dynamical model with two degrees of freedom (angle of rotation around the center of gravity $\theta(t)$ and vertical displacement $y(t)$) that will interact with the fluid through aerodynamical forces exerted on the structure and used to update the structure position.

We suppose that there exist a reference configuration (Ω_S^0, $\Gamma_{F/S}^0$, Ω_F^0) that can be associated with the actual configuration ($\Omega_S^m(t)$, $\Gamma_{F/S}^m(t)$, $\Omega_F^m(t)$) at each instant t (see Figure 5).

In other words, to each $\xi \in \Omega_F^0$ we can associate $x \in \Omega_F^m(t)$ defining the transformation

$$x = x(\xi, t) \tag{23}$$

The Jacobian of the transformation J and the velocity of the transformation w are defined as

$$J = \det\left(\left.\frac{\partial x}{\partial \xi}\right|_t\right), \qquad w = \left.\frac{\partial x}{\partial t}\right|_\xi \tag{24}$$

3.1. Injection/suction boundary conditions

The aim is to take into account the small changes in the shape (position) of the structure through the boundary conditions applied on the reference configuration (as the flow domain).

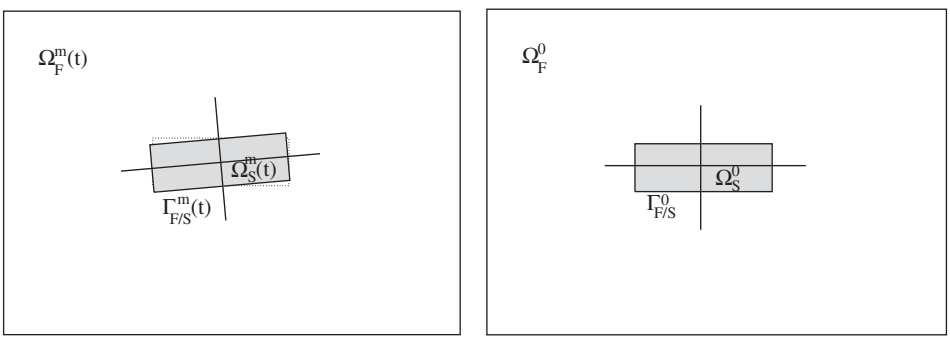

Figure 5. Problem definition: actual configuration (left), reference configuration (right).

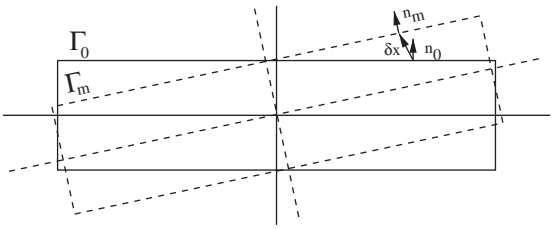

Figure 6. Injection/suction boundary conditions.

This approximation reduces the cost of the numerical simulation significantly as it restricts all influence of the change of the shape of the fluid domain $\Omega_F^m(t)$ just on the boundary conditions imposed on $\Gamma_{F/S}^0$ (see also References [31, 16, 18, 19]).

3.1.1. Injection boundary condition. After a Taylor expansion around the original shape (see Figure 6, we have

$$U_m \cdot n_m = U_0 \cdot n_0 + \delta x \cdot \nabla(U_0 \cdot n_0) + O(|\delta x|^2) \tag{25}$$

where subscript m represents the actual moving shape and 0 the shape of reference (fixed), $n_{0,m}$ are the unit normals on each shape, and δx is the vector of shape deformation. At first order, using $\delta x \cdot \nabla(U_0 \cdot n_0) = \delta x \cdot \nabla U_0 \cdot n_0 + \delta x \cdot \nabla n_0 \cdot U_0$ together with $\delta x \cdot \nabla n_0 \cdot U_0 \approx U_0 \cdot (n_m - n_0)$ we have:

$$U_m \cdot n_m = U_0 \cdot n_0 + U_0 \cdot (n_m - n_0) + \delta x \cdot \nabla U_0 \cdot n_0 \tag{26}$$

If we suppose that for a small variation of the shape, U remains almost unchanged while the normal to the shape has variation of the same order (i.e. $|\delta x| \approx |\delta n| \approx O(1)$, but $|\delta u| \approx O(\varepsilon)$, $u_0 \approx u_m$), we have:

$$U_m \cdot n_m = U_0 \cdot n_0 + U_0 \cdot (n_m - n_0) \tag{27}$$

Since we are analysing the problem in the fixed frame of reference, we have to take into account the velocity of the shape (given by the movement definition in the context of forced movement, or computed at every instant in the aeroelastic simulation). This changes the boundary condition on $\Gamma_m : U_m \cdot n_m = 0$ in $U_m \cdot n_m = w \cdot n_m$ with w the velocity of the shape.

Finally, the injection/suction boundary condition we impose on Γ_0 is:

$$U_0 \cdot n_0 = w \cdot n_m - U_0 \cdot (n_m - n_0) \tag{28}$$

To improve the accuracy, we can substitute the truncated formula (27) with the complete expression (26), leading to the following injection/suction boundary condition on Γ_0:

$$U_0 \cdot n_0 = w \cdot n_m - U_0 \cdot (n_m - n_0) - \delta x \cdot \nabla U_0 \cdot n_0 \tag{29}$$

This is an implicit relation on U_0. We can use a fixed point method:

$$U_0^{n+1} \cdot n_0 = w^{n+1} \cdot n_m^{n+1} - U_0^n \cdot (n_m^{n+1} - n_0) - \delta x^{n+1} \cdot \nabla U_0^n \cdot n_0 \tag{30}$$

3.1.2. No-slip boundary condition. In the context of viscous flow simulation we have to satisfy the condition $U_m = w$.

Using the same approach as in (26), we can develop the boundary condition for tangential velocity

$$U_0^{n+1} \cdot s_0 = w^{n+1} \cdot s_m^{n+1} - U_0^n \cdot (s_m^{n+1} - s_0) - \delta x^{n+1} \cdot \nabla U_0^n \cdot s_0 \tag{31}$$

and use it together with (30) for laminar flow simulations.

3.1.3. Wall-laws. Still, since we are interested in the simulation of turbulent flow, we do not solve our fluid problem up to the wall Γ_w but we use the wall-laws (6)–(7) on Γ_δ instead.

We will use the same technique as used in our explicit solver NSIKE for fixed geometry, where we use $U^n \cdot s$ to compute the friction velocity $(u_\tau)^n$ from Reichardt equation. $(u_\tau)^n$ is then used in the computation of boundary conditions at $n+1$ step where we need $(S \cdot n \cdot s)^n$ (since we use explicit time integration and we integrate the boundary integral explicitly), k^{n+1} and ε^{n+1}.

In the case of moving boundary, we compute $(S_m \cdot n_m \cdot s_m)^n$, k_m^{n+1} and ε_m^{n+1} using the wall-laws (6)–(7) from $(u_\tau^m)^n$ that is here computed from

$$\frac{U_m \cdot s_m - w \cdot s_m}{u_\tau^m} = 2.5 \ln(1 + \kappa y^+) + 7.8 \left(1 - \mathrm{e}^{-y^+/11} - \frac{y^+}{11} \mathrm{e}^{-0.33 y^+}\right) \tag{32}$$

where $U_m \cdot s_m$ has to be reconstructed from $U_0 \cdot s_0$ using

$$U_m \cdot s_m = U_0 \cdot s_0 + \delta x \cdot \nabla (U_0 \cdot s_0) \tag{33}$$

Note that in these expressions U_m denotes the velocity at $\Gamma_{m,\delta}$, i.e. the velocity on the fictitious boundary at the distance δ from the moving boundary Γ_m (we apply the standard wall-laws technique), and, therefore, $U_m \neq w$.

In the above expression it is important to note that the constants values have been chosen to satisfy the experiments on the fixed flat plate (and not the moving one).

Finally, new boundary conditions applied on the boundary of the configuration of reference $\Gamma_{0,\delta}$ are computed using:

$$(S_0 \cdot n_0 \cdot s_0) = (S_m \cdot n_m \cdot s_m) - \delta x \cdot \nabla (S_0 \cdot n_0 \cdot s_0) \tag{34}$$

$$k_0 = k_m - \delta x \cdot \nabla k_0 \tag{35}$$

$$\varepsilon_0 = \varepsilon_m - \delta x \cdot \nabla \varepsilon_0 \tag{36}$$

These are implicit relations and we can use the same approach as for $U_0 \cdot n$ in (30), i.e. a fixed point method.

We remark that at this stage we have supposed $U_m \cdot s_m = U_0 \cdot s_0$ in (33), and $S_0 \cdot n_0 \cdot s_0 = S_m \cdot n_m \cdot s_m$, $k_0 = k_m$, $\varepsilon_0 = \varepsilon_m$ in (34)–(36).

These conditions are widely used to represent shape deformation and avoid an ALE formulation [16] in control and optimization problems.

3.2. ALE formulation (dynamic mesh method)

The ALE formulation is a formulation used for the domains with moving boundaries. Here we will consider a special class of ALE formulations, the dynamic mesh method (see References [9–15]).

Providing that we may specify in some way the distribution of the mesh velocity $w(x,t)$ in $\Omega_F(t)$ in accordance with the motion of $\Omega_F(t)$, we may employ the following ALE description of the Navier–Stokes equations as the governing equations of fluid motion [9] in $\Omega_F(t)$:

$$\nabla \cdot U = 0 \tag{37}$$

$$\partial_t U + (U - w) \cdot \nabla U + \nabla P/\rho - \nabla \cdot ((\nu + \nu_t)(\nabla U + \nabla U^T)) = 0 \tag{38}$$

$$\partial_t k + (U - w) \cdot \nabla k - \nabla \cdot ((\nu + \nu_t)\nabla k) = S_k \tag{39}$$

$$\partial_t \varepsilon + (U - w) \cdot \nabla \varepsilon - \nabla \cdot ((\nu + c_\varepsilon \nu_t)\nabla \varepsilon) = S_\varepsilon \tag{40}$$

The algorithm for ALE formulation in our incompressible solver NSIKE consists in the following steps (see also Reference [31]):

Step 1: First of all, we will update the position of the moving part of the boundary (usually Γ_{3h}). This is done according to the fluid–structure interaction algorithm we are using, typically we pass the new position (shape) of the structure computed separately (for instance, forced movement or simple several degrees of freedom integration).

Then we have to compute the new mesh corresponding to the new shape of the domain $\Omega_F(t)$. Once the change in the position of boundary nodes δx_w (nodes situated on the boundary Γ) is known, we have to expand these variations overall the mesh. We have chosen to do that using the following formula based on the distance of the mesh nodes x_i to the boundary nodes x_w (see Reference [33]):

$$\delta x_i = \frac{1}{\int_\Gamma \mathrm{d}\gamma/|x_i - x_w|^\beta} \int_\Gamma \frac{\delta x_w}{|x_i - x_w|^\beta}\,\mathrm{d}\gamma \tag{41}$$

where Γ is the flow domain boundary and $\beta \geqslant 2$. The above approach proved to be more robust when treating extremely fine meshes than the approach based on solving a volumic elasticity system to propagate the boundary deformation [19].

Finally, all the geometrical quantities have to be recomputed, including the mesh velocity (i.e. the velocity of nodal movement):

$$w_i^{n+1} = \frac{1}{\Delta t}(x_i^{n+1} - x_i^n) \tag{42}$$

Step 2: The intermediate velocity is now computed using the formulation

$$\frac{1}{\Delta t}(M^{n+1}\tilde{U}^{n+1} - M^n U^n) + (B^n(U^n - w^n) + B^{*n}(U^n))U^n + C^n U^n - \Sigma^n = 0 \tag{43}$$

where

$$M_{mn} = (\phi_{i,j}, \phi_{k,l}), \qquad B_{mn} = ((U_h^n - w_h^n) \cdot \nabla \phi_{i,j}, \phi_{k,l}) \tag{44}$$

$$B^*_{mn} = \sum_K (U_h^n \cdot \nabla \phi_{i,j}, g_1^K)_K, \quad C_{mn} = ((\nu + \nu_t^n)(\nabla \phi_{i,j} + \nabla \phi_{i,j}^{\mathrm{T}}), \nabla \phi_{k,l}) \tag{45}$$

$$\sum_m = \int_{\Gamma_{3h}} S_t^n \cdot n \cdot \phi_{k,l} \tag{46}$$

with $m = (k-1)d + l$ and $n = (i-1)d + j$.

For k and ε we have the following similar formulation:

$$\frac{1}{\Delta t}(M^{n+1}k^{n+1} - M^n k^n) + (B^n(U^n - w^n) + B^{*n}(U^n, k^n))k^n + C^n k^n - S_k^n(U^n, k^n, \varepsilon^n) = 0 \tag{47}$$

$$\frac{1}{\Delta t}(M^{n+1}\varepsilon^{n+1} - M^n \varepsilon^n) + (B^n(U^n - w^n) + B^{*n}(U^n, \varepsilon^n))\varepsilon^n + C^n \varepsilon^n - S_\varepsilon^n(U^n, k^n, \varepsilon^n) = 0 \tag{48}$$

where the matrices are defined as

$$M_{ij} = (\psi_j, \psi_i), \qquad B_{ij} = ((U_h^n - w_h^n) \cdot \nabla \psi_j, \psi_i), \qquad B^*_{ij} = \sum_K (U_h^n \cdot \nabla \psi_j, g_2^K)_K \tag{49}$$

$$C_{ij} = ((\nu + \nu_t^n)\nabla \psi_j, \nabla \psi_i), \qquad (S_k)_i = (S_{kh}^n, \psi_i), \qquad (S_\varepsilon)_i = (S_{\varepsilon h}^n, \psi_i) \tag{50}$$

The notation M^{n+1}, for example, indicates that the integrals in the computation of matrix M components are computed over the domain $\Omega(t)$ at the instant t in time corresponding to the $n+1$ step of our time integration loop.

As stated before, the mass matrices M are lumped to have completely decoupled explicit system for $\tilde{U}^{n+1}$, k^{n+1} and ε^{n+1}, and corrections are introduced to take into account the Dirichlet boundary conditions. Note that the velocity of the mesh w affects only the Galerkin part of the convective term formulation [8].

Step 3: We solve on Ω_h^{n+1}

$$C^{n+1}\Phi^{n+1} = F^{n+1}(\tilde{U}^{n+1}) \tag{51}$$

where Φ^{n+1} is the vector of nodal values of φ_h^{n+1}, C_{ij}^{n+1} is defined as in (50) and

$$F_i = (\nabla \cdot \tilde{U}_h^{n+1}, \psi_i) \tag{52}$$

together with corrections allowing to take into account the Dirichlet boundary conditions.

Step 4: Finally, we update the velocity field taking into account the pressure gradient:

$$M^{n+1}V^{n+1} = M^n \tilde{U}^n - P^{n+1}\Phi^{n+1} \tag{53}$$

where M_{mn}^{n+1} is defined as in (44)

$$P_{mi} = (\nabla \psi_i, \phi_{k,l}) \tag{54}$$

where $m = (k-1)d + l$.

As boundary conditions even with ALE simulation we used wall-laws, where we computed $(S_m \cdot n_m \cdot s_m)^n$, k_m^{n+1} and ε_m^{n+1} from $(u_\tau^m)^n$ which is computed solving directly (32). We have also carried out tests using ALE formulation coupled with two-layer strategy for treating near wall region, using the boundary conditions $U_m = w$. These results confirm rather well the results obtained using wall-laws technique (see Reference [31]).

Here we have to remark that the CPU-time needed for one iteration of the numerical simulation using ALE formulation is at least double with respect to the one needed when using injection/suction boundary conditions instead. This very important increase in the cost of the simulation is due to the need of recalculation of all geometrical quantities at each iteration step of our solver NSIKE (based on explicit time integration).

One possibility to diminish the cost of ALE simulation would be to reconstruct the geometry after each N time iteration steps, instead of doing it at each time step.

This is equivalent to an implicit ALE scheme where for each time step Δt, we do a sub-cycling with N flow iterations with time step given by the stability condition $\mathrm{d}t$, such that $N\,\mathrm{d}t = \Delta t$. In that case, the cost of the ALE simulation becomes equivalent to the fixed domain simulation cost plus the cost of the mesh deformation every N iterations.

Another important point considering ALE simulation is the eventual problem of mesh distortion. For a given problem, we can arrive at a mesh-independent solution giving a suitable mesh, but if we subject this mesh to rotation of several degrees the mesh deformation, especially in the vicinity of sharp edges, this can lead to a certain loss in the accuracy.

3.3. Tests for injection/suction boundary conditions

3.3.1. NACA-0012 profile. The *first test* concerns the analysis of incompressible turbulent attached flow over a well-profiled body such as NACA-0012 profile.

We consider the flow at $Re_c = 100\,000$, using NSIKE solver, with k–ε model and wall-laws with $\delta = 0.01c$ (where c is the profile chord) in wall-laws, giving y^+ values between 20 and 30. The mesh used in the computations consisted in 2151 nodes and 4171 elements, although we tested finer meshes to establish the mesh dependence of results (no major differences were observed with further refinement—the flow is incompressible and attached).

First, we analyse the flow for the profile at incidence 2° and compare the results obtained with the profile at incidence 0° and the change in the profile position taken into account through the injection/suction boundary conditions (28), that we will refer as truncated formula, and (29). The pressure distribution on the profile is shown in Figures 7 and 8. The computed drag C_D and lift C_L coefficients differ in about than 10%.

For this case, we carried out the computations even with our compressible solver NSC2KE [21] to see the effect of the numerical techniques specific for the incompressible solver NSIKE: projection method and the boundary condition $U \cdot n$ treated in the strong sense (while in the compressible case they are treated in the weak sense). The pressure distribution computed with the injection/suction boundary conditions in the compressible solver agrees better with the 2° incidence solution, than when doing incompressible computations. Even more, the differences between the truncated formula for $U \cdot n$, and the complete injection/suction boundary condition

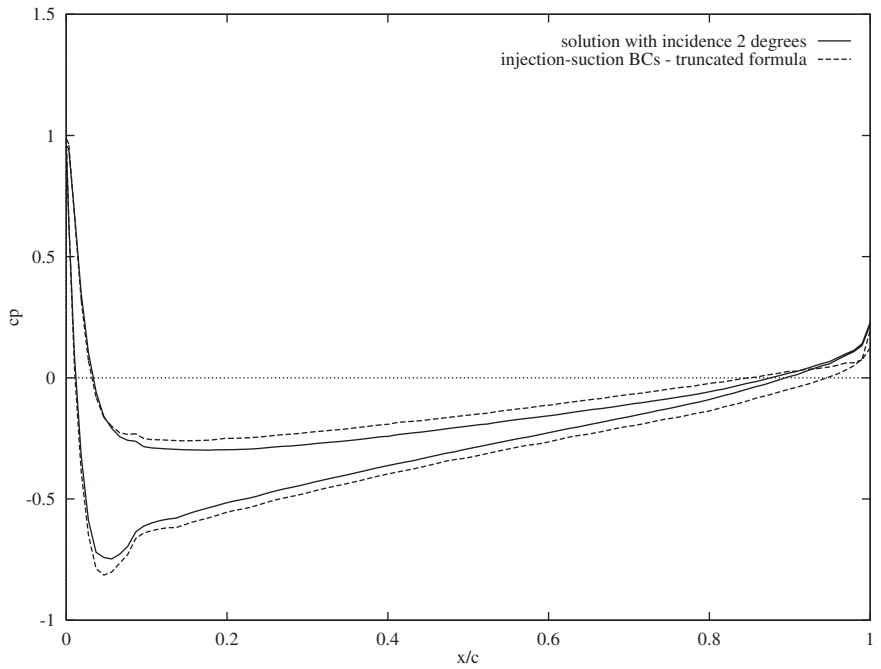

Figure 7. NACA-0012 profile at incidence 2°, $Re_c = 100\,000$.

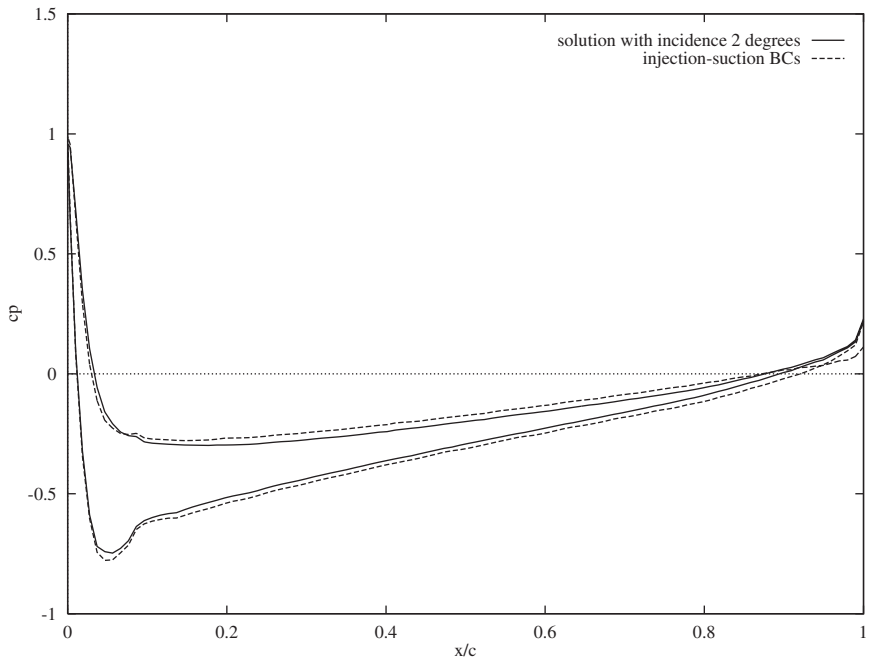

Figure 8. NACA-0012 profile at incidence 2°, $Re_c = 100\,000$.

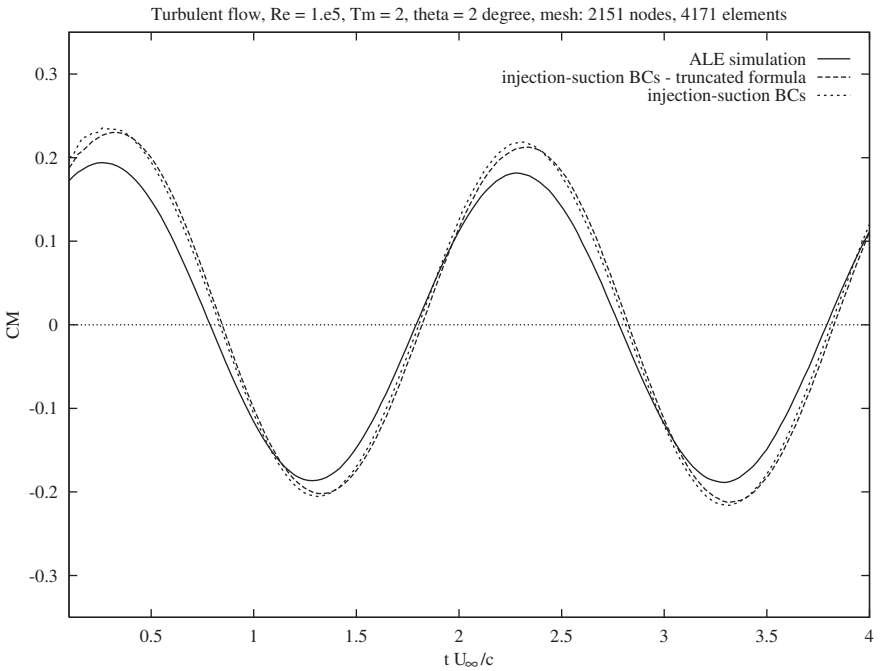

Figure 9. NACA-0012 profile at incidence -2°, $Re_c = 100\,000$, $u^* = u_\infty T/c = 2$.

are less important. And finally, the differences in the computed drag C_D and lift C_L coefficients differ in less than 5%. When analysing pressure distribution coming from the incompressible solver NSIKE computations, we can remark that the deviation is the most important close to the trailing edge (that can imply that the treatment of $U \cdot n$ in the strong sense at the trailing edge is responsible for those problems).

The *second test* consisted in imposing a periodic movement to the profile

$$\theta(t) = A \sin(2\pi t/T_m) \tag{55}$$

where θ is the angle of rotation around the center of gravity and A the amplitude (chosen 2°) and T_m the period of oscillations (we have chosen different values). Here, we have performed computations using both the ALE formulation and the injection/suction boundary conditions. Typical oscillations of the moment coefficient computed with different techniques C_M are shown in Figure 9.

In Table I below, we have summarized the amplitudes and the phase shift of oscillations of computed aerodynamic moment $M(t) = M_0 \sin(2\pi f_m t + \beta)$, computed using injection/suction boundary conditions with respect to the ones computed using ALE formulation for different frequencies of imposed movement ($u^* = u_\infty/c\, f = u_\infty T/c$).

3.3.2. Rectangle profile. The next step is the analysis of unsteady incompressible turbulent flow over a rectangle profile ($c/d = 4$) for $Re_d = 20\,000$, already considered before.

Table I. NACA-0012 profile in forced movement.

	$u^*=0.5$	$u^*=1.0$	$u^*=2.0$	$u^*=5.0$	$u^*=10.0$
ALE	$M_0,\ \beta$	$M_0,\ \beta$	$M_0,\ \beta$	$M_0,\ \beta$	$M_0,\ \beta$
Injection/suction BCs	$1.29M_0,$ $\beta+0.014T$	$1.24M_0,$ $\beta+0.018T$	$1.2M_0,$ $\beta+0.018T$	$1.14M_0,$ $\beta+0.02T$	$1.05M_0,$ $\beta+0.02T$
Injection/suction BCs truncated	$1.28M_0,$ $\beta+0.03T$	$1.22M_0,$ $\beta+0.032T$	$1.18M_0,$ $\beta+0.04T$	$1.145M_0,$ $\beta+0.044T$	$1.06M_0,$ $\beta+0.05T$

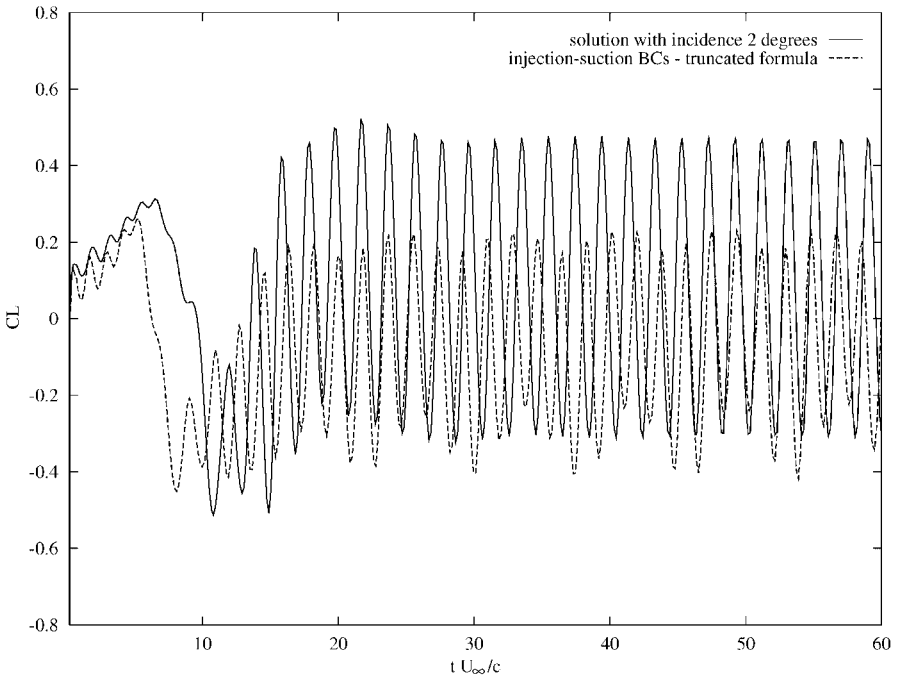

Figure 10. Rectangle profile at incidence 2°, $Re_d = 20\,000$.

Here we are interested in the flow computed for that profile fixed at incidence 2° compared to the one obtained with the profile at incidence 0° using injection/suction boundary conditions to take into account the change in the profile position. The flow over a rectangle profile is unsteady, with multiple recirculation zones. This represents a more complex test for our approximations in injection/suction boundary conditions than the completely attached flow over a NACA-0012 profile. The lift coefficient C_L obtained using injection/suction boundary conditions is shown in Figures 10 and 11.

The solution for the profile fixed at 2° incidence gives $\bar{C}_L = 0.075$, while the result from injection/suction boundary conditions is about $\bar{C}_L = 0.015$. The truncated formula for $U_0 \cdot n_0$

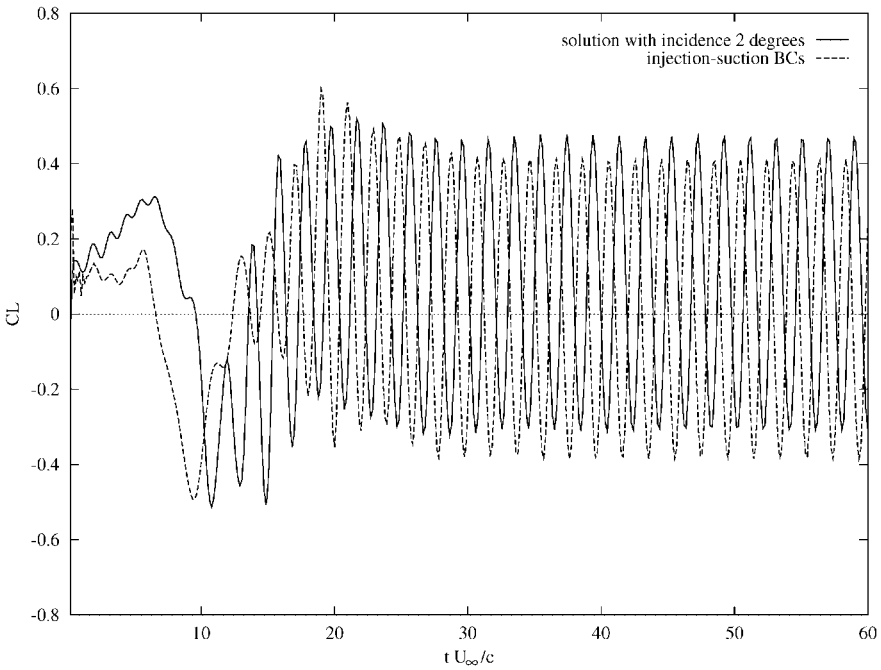

Figure 11. Rectangle profile at incidence 2°, $Re_d = 20\,000$.

in injection/suction boundary conditions gives negative values of $\bar{C}_L = -0.09$ with much more unstable behaviour than the two other computations.

4. FLUID–STRUCTURE INTERACTION SIMULATIONS

After the first tests with injection/suction boundary conditions, we proceed with the analysis of the response of the structure to forced oscillations. The second step is the analysis of the behaviour of the structure when associated with a simple dynamical model with two degrees of freedom.

4.1. Forced movement

When studying dynamical behaviour of a fluid–structure system, one approach consists of analysing the response of the system to forced perturbation without taking into account any dynamics model. In this approach, we impose a movement for the bridge or viaduct cross-section and the hysteresis curves are used to predict the response of the real elastic system by means of engineering criteria (see Reference [1]).

In the context of forced movement, we consider a rectangular viaduct cross-section with width/height ratio $c/d = 4$ for which experimental results are available.

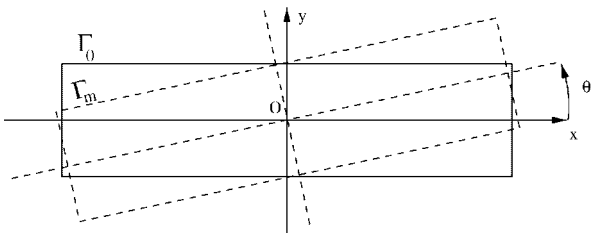

Figure 12. Torsional oscillations.

4.1.1. Torsional oscillations for rectangle profile. We prescribe a periodic torsional oscillation around the cross-section centre of gravity (Figure 12):

$$x_m = R(t)x_0, \qquad (n_m = R(t)n_0) \tag{56}$$

where $R(t)$ is a rotation matrix:

$$R(t) = \begin{bmatrix} \cos\theta & -\sin\theta \\ \sin\theta & \cos\theta \end{bmatrix} \tag{57}$$

The angle of rotation is defined as $\theta(t) = \theta_0 \cos(2\pi t/T_m)$, where θ_0 is chosen 1.91° and the period of oscillations T_m is chosen to have values of $u^* = u_\infty/df_m = u_\infty T_m/d$ ranging from 5 to 40.

Engineering criterium (e.g. the theory of Scanlan, see Reference [1]) used to estimate the stability of the cross-section profile is based on the extraction of the response of the system (here, the aerodynamic moment M_m) at the perturbation frequency $f_m = 1/T_m$:

$$M_m(t) = M_0 \cos(2\pi f_m t + \beta) \tag{58}$$

We compute

$$\begin{bmatrix} a_m \\ b_m \end{bmatrix} = \frac{1}{NT_m} \int_{-NT_m}^{NT_m} M(t) \begin{bmatrix} \cos(2\pi f_m t) \\ \sin(2\pi f_m t) \end{bmatrix} \mathrm{d}t \tag{59}$$

where $M(t)$ is the obtained aerodynamic moment.

The comparison of the computed coefficients

$$C_{mR} = \frac{a_m}{\frac{1}{2}\rho|u_\infty|^2 c^2 l}, \quad C_{mI} = \frac{-b_m}{\frac{1}{2}\rho|u_\infty|^2 c^2 l} \tag{60}$$

with the experimental results is given in Figures 13 and 14.

The response of the system at the perturbation frequency is estimated as [1–3]:

$$M_m(t) = \frac{1}{2}\rho|u_\infty|^2 c^2 l \left(\frac{C_{mR}}{\theta_0}\theta(t) + \frac{C_{mI}}{\theta_0 2\pi f_m}\dot{\theta}(t) \right) \tag{61}$$

where the system is unstable when the coefficient C_{mI} becomes positive.

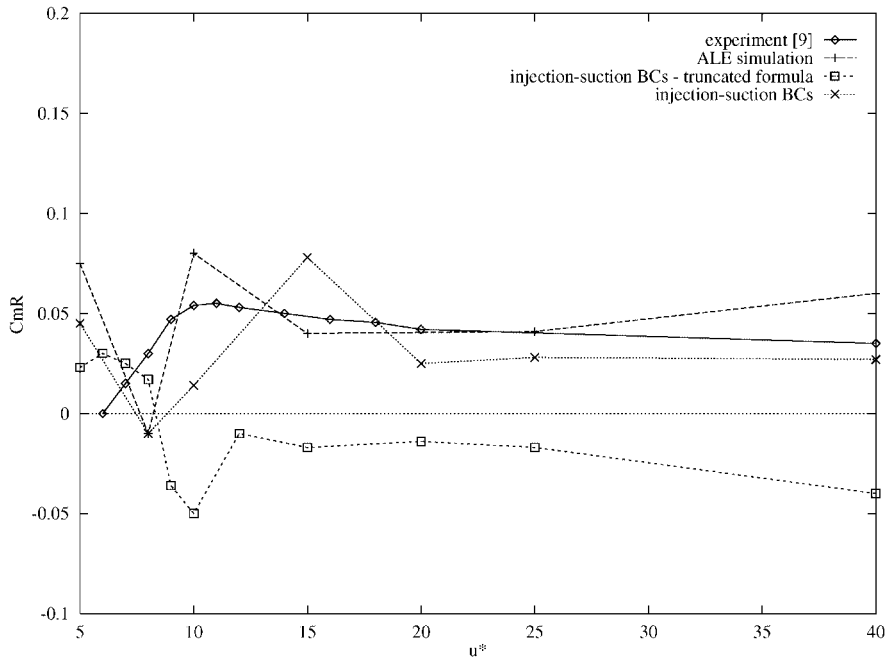

Figure 13. Torsional oscillations, rectangle profile, $Re_d = 20\,000$, C_{mR} vs $u^* = u_\infty/df$.

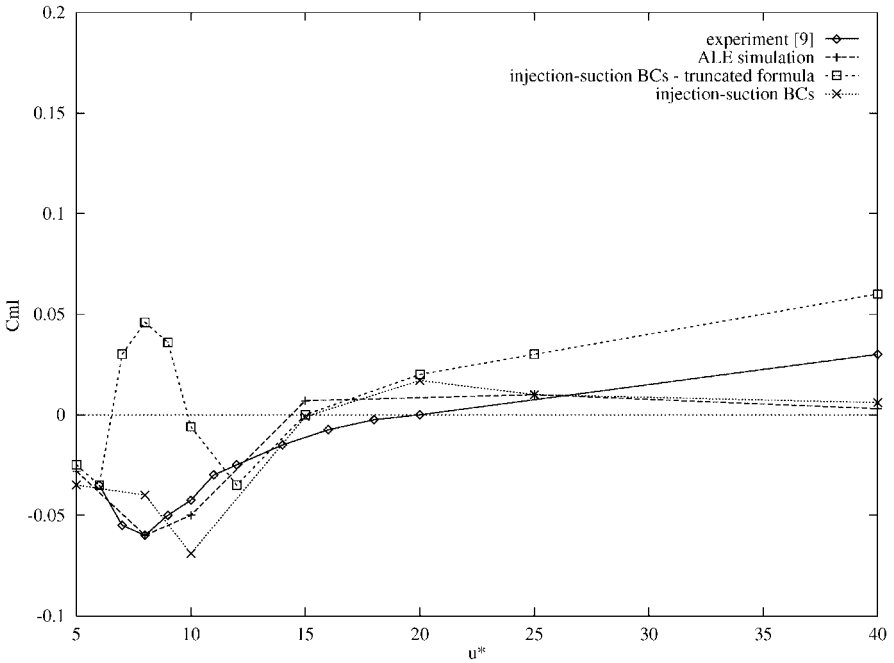

Figure 14. Torsional oscillations, rectangle profile, $Re_d = 20\,000$, C_{mI} vs $u^* = u_\infty/df$.

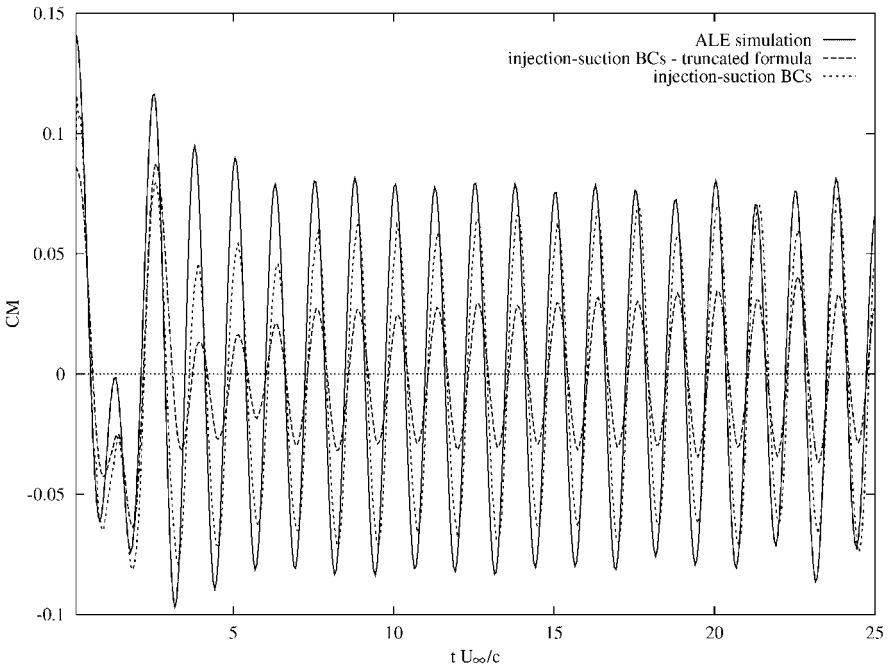

Figure 15. Torsional oscillations for rectangle profile, $Re_d = 20\,000$, $u^* = u_\infty/df = 5$.

When analysing the results of numerical simulations, the diagram of main interest is the one presenting the values of C_{mI} coefficient with respect to different frequencies of forced movement, i.e. different values of non-dimensionalized velocity $u^* = u_\infty/df$, Figure 14.

It is important to remark that even the experimental results seem contradictory, because of the fact that for big values of u^* (quasi-static situation) the coefficient C_{mI} values should have zero as an asymptotic value. The results from three simulations, using ALE formulation, using injection/suction boundary conditions with truncated formula for $U \cdot n$, and using the complete injection/suction boundary conditions, vary significantly. Nevertheless, there is better agreement between complete injection/suction boundary conditions with ALE formulation simulations (the trends seem rather similar).

On the other hand, both, tests carried out before for injection/suction boundary conditions, together with these results, indicate that the truncated formula for $U \cdot n$ seems not to be a good approximation for these vortex shedding flows, except for high frequency perturbations, i.e. when the term $w \cdot n_m$ dominates in (29). However, when treating attached flows like flows over NACA airfoils, there is less differences between two injection/suction formula for $U \cdot n$.

The effect of neglecting the term ∇U in injection/suction boundary conditions for $U \cdot n$ can be seen in Figures 15 and 16.

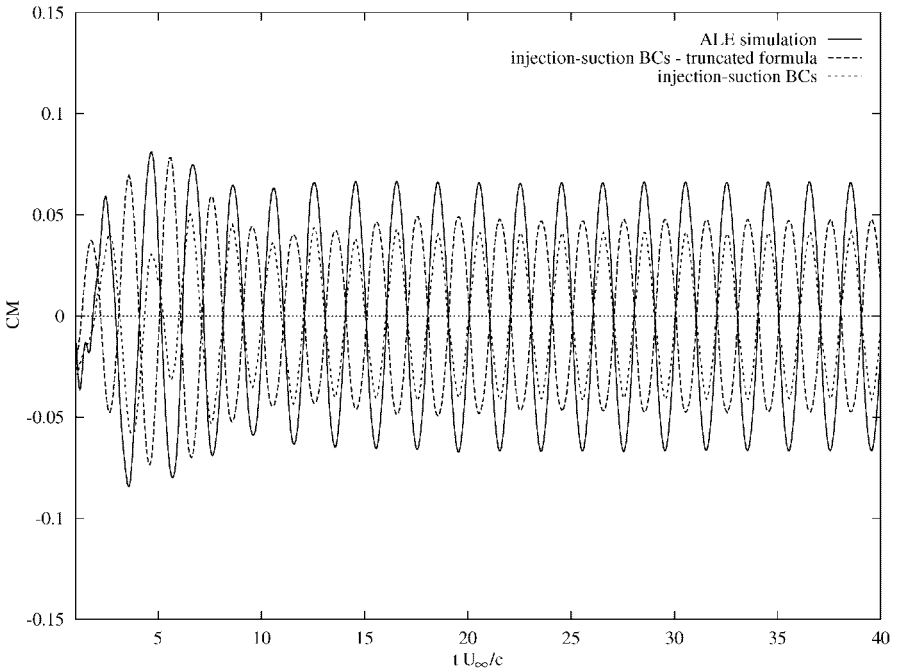

Figure 16. Torsional oscillations for rectangle profile, $Re_d = 20\,000$, $u^* = u_\infty/df = 8$.

4.2. Rigid body dynamics for structure

The second step is an attempt to take into account the realistic dynamic behaviour of the system. This is done through the following two DOF system:

$$J\frac{\mathrm{d}^2X}{\mathrm{d}t^2} + C\frac{\mathrm{d}X}{\mathrm{d}t} + K(X - X^0) = F \tag{62}$$

where $X = [y, \theta]^{\mathrm{T}}$ (X^0 being the initial configuration) the torsional rotation and vertical displacement, $F = [F_{\mathrm{L}}, F_M]^{\mathrm{T}}$ are the corresponding aerodynamic forces. J, C and K describe the mechanical characteristics of the structure:

$$J = \begin{bmatrix} m & S_\theta \\ S_\theta & I_\theta \end{bmatrix}, \qquad C = \begin{bmatrix} c_y & 0 \\ 0 & c_\theta \end{bmatrix}, \qquad K = \begin{bmatrix} k_y & 0 \\ 0 & k_\theta \end{bmatrix}$$

where m and I_θ are the mass and the inertial moment of the profile, S_θ is the static moment of the profile, c_y, c_θ are the damping coefficients, and k_y, k_θ are the stiffness coefficients.

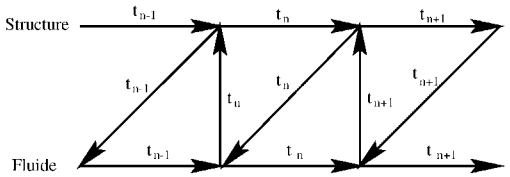

Figure 17. Fluid–structure interaction algorithm.

We use the Newmark's method (the trapezoidal rule) for the integration in time of the system (62):

$$\begin{aligned} \dot{Z}(t) &= f(t, Z) \\ Z(t=0) &= Z_0 \end{aligned} \tag{63}$$

where

$$Z = \begin{bmatrix} X \\ \dot{X} \end{bmatrix}$$

are the new variables, and

$$f(Z,t) = \begin{bmatrix} \dot{X} \\ J^{-1}F - J^{-1}C\dot{X} - J^{-1}KX \end{bmatrix}$$

The numerical scheme is

$$\begin{aligned} Z_0 &= Z(t=0) \\ Z_{n+1} &= Z_n + \triangle t \frac{f(t_n, Z_n) + f(t_{n+1}, Z_{n+1})}{2} \end{aligned} \tag{64}$$

In the context of injection/suction boundary conditions, at each time step we use the predicted lift and moment aerodynamic coefficients to advance in time the system (64) and use the values of the displacements X to provide the new boundary condition for $(u_0 \cdot n_0)$ as indicated schematically in Figure 17.

4.2.1. Fluid–structure interaction simulation for rectangle profile. We analysed the same rectangular profile used in the forced movement computations ($c/d = 4$). For the mechanical characteristics of this profile (see also Reference [31]) we have chosen the ones representing a 'rough' approximation of the bridge over Rio Niteroi in Brazil (with $d = 3m$): $m = 20\,\mathrm{t\,m^{-1}}$, $k_y = m\omega_y^2$, $\omega_y = 2\pi f_y = 20\,\mathrm{s^{-1}}$, $I_\theta = 400\,\mathrm{t\,m}$, $k_\theta = I_\theta \omega_\theta^2$, $\omega_\theta = 2\pi f_\theta = 50\,\mathrm{s^{-1}}$ and the damping coefficients c_y, c_θ were neglected, as well as the coupling of the vertical and torsional oscillations (S_θ). We used maximum wind velocities $u_\infty = 150\,\mathrm{km\,h^{-1}}$, giving $Re_d \approx 10^7$.

Here we present only the results obtained for one degree of freedom, angle of rotation θ, in order to compare them to the stability analysis in the case of imposed torsional oscillations [1–3]. More results for the system with two degrees of freedom can be found in Reference [31].

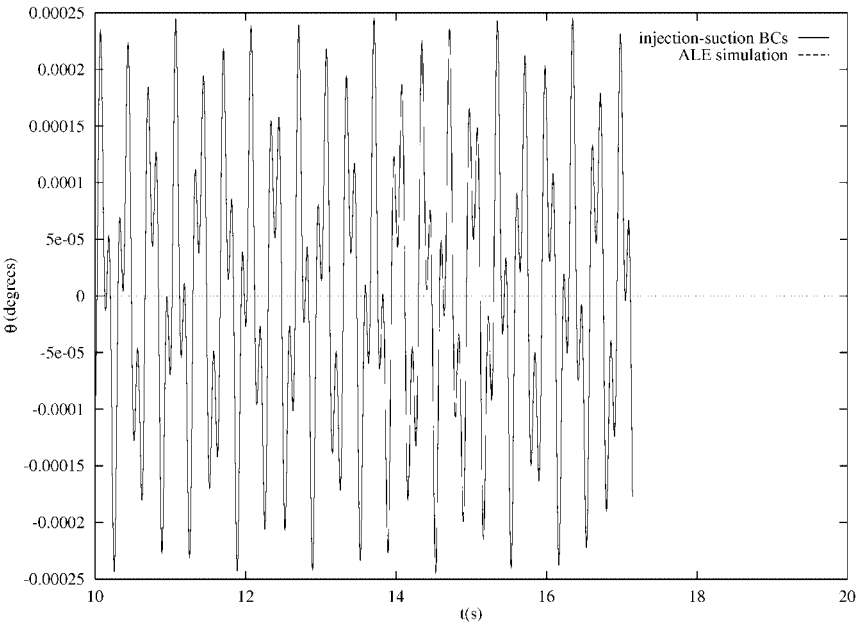

Figure 18. Fluid–structure interaction simulation, $Re_d = 10^7$, $u_\theta^* = u_\infty / df_\theta = 1.75$. Computations with original mechanical characteristics.

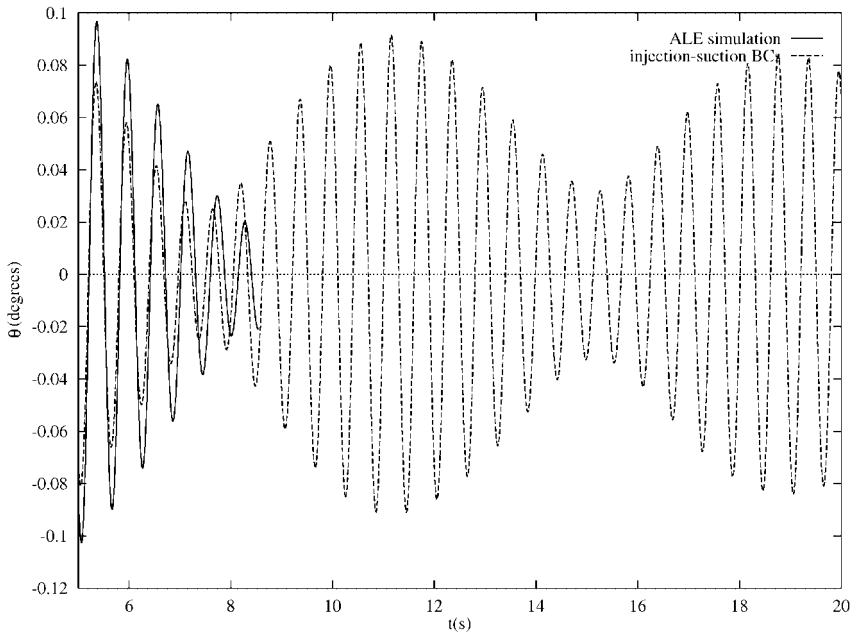

Figure 19. Fluid–structure interaction simulation, $Re_d = 10^7$, $u_\theta^* = u_\infty / df_\theta = 8.75$, $I_\theta = 40\,\mathrm{t\,m}$, $\omega_\theta = 10\,\mathrm{s}^{-1}$. ALE simulation and injection/suction boundary conditions predict similar regime.

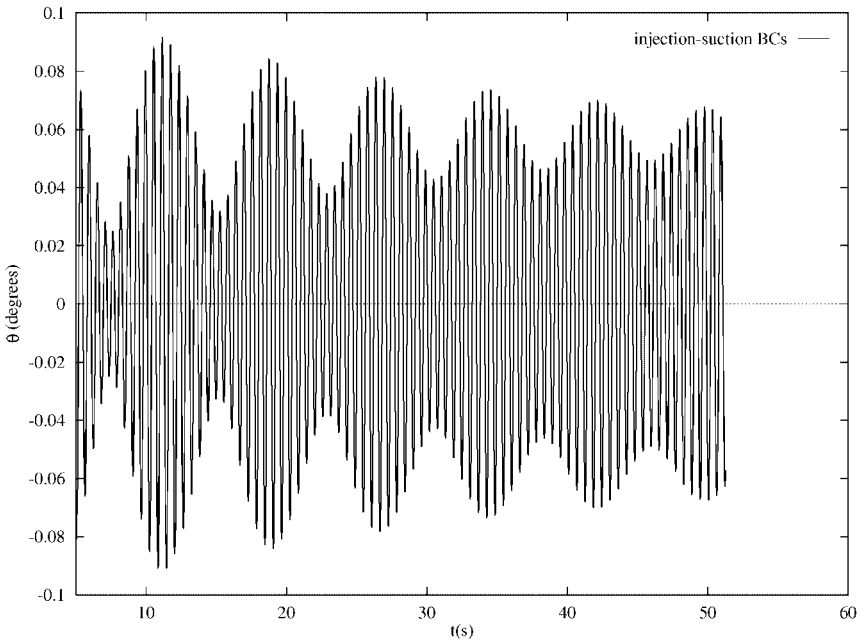

Figure 20. Fluid–structure interaction simulation, $Re_d = 10^7$, $u_\theta^* = u_\infty / df_\theta = 8.75$, $I_\theta = 40\,\mathrm{t\,m}$, $\omega_\theta = 10\,\mathrm{s}^{-1}$. Long time simulation using injection/suction boundary conditions.

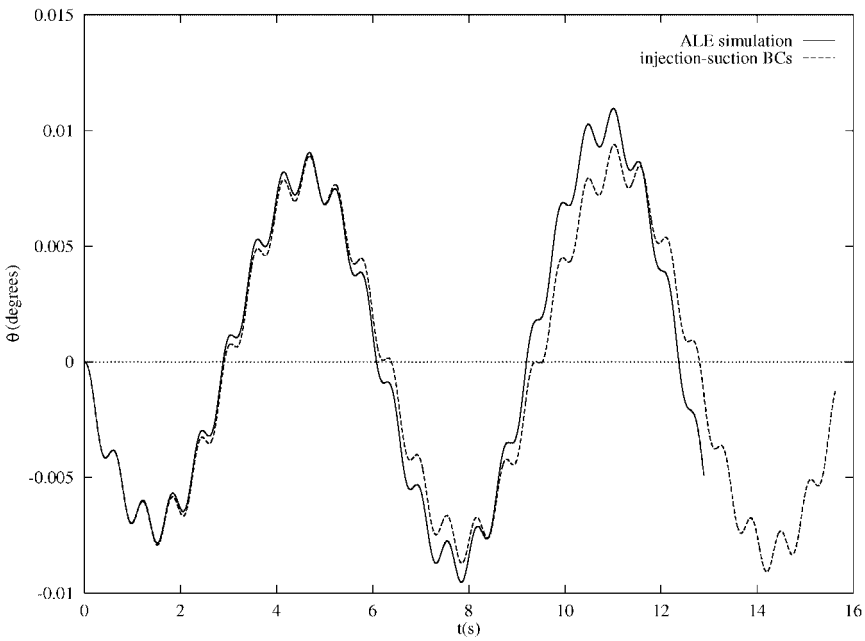

Figure 21. Fluid–structure interaction simulation, $Re_d = 10^7$, $u_\theta^* = u_\infty / df_\theta = 87.5$, $\omega_\theta = 1\,\mathrm{s}^{-1}$. Both, ALE simulation and injection/suction boundary conditions predict similar unstable regime.

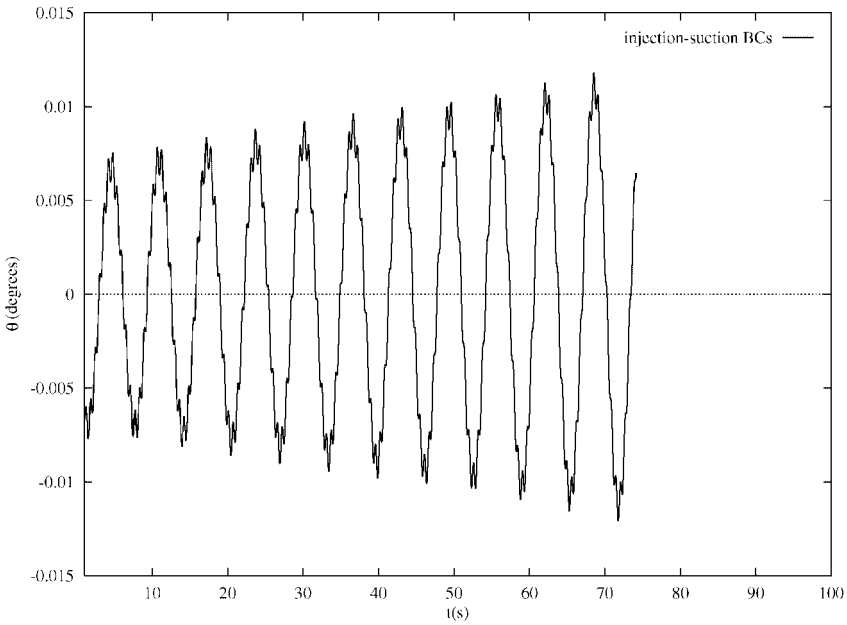

Figure 22. Fluid–structure interaction simulation, $Re_d = 10^7$, $u_\theta^* = u_\infty / df_\theta = 87.5$, $\omega_\theta = 1\,\mathrm{s}^{-1}$. Long time simulation using injection/suction boundary conditions.

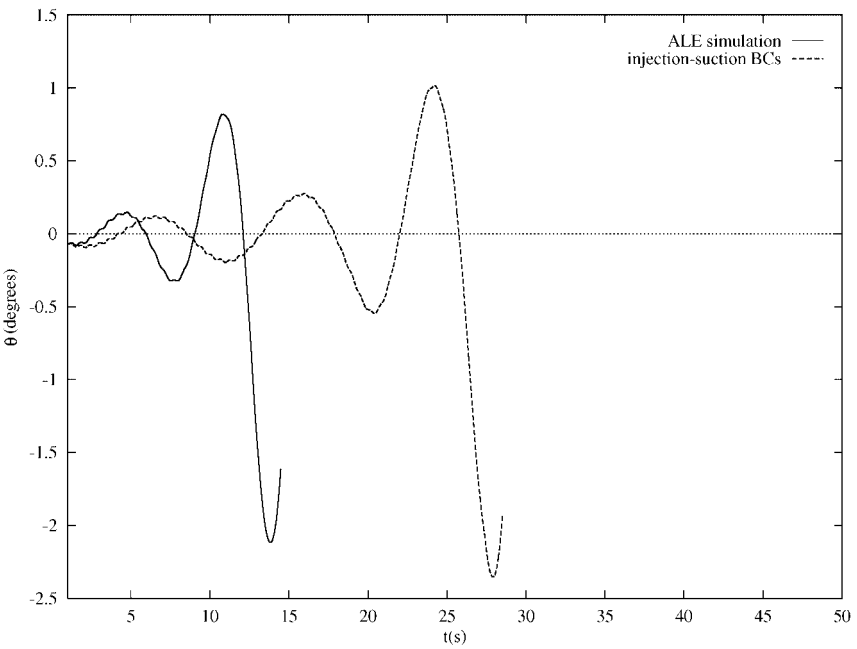

Figure 23. Fluid–structure interaction simulation, $Re_d = 10^7$, $u_\theta^* = u_\infty / df_\theta = 87.5$, $I_\theta = 40\,\mathrm{t\,m}$, $\omega_\theta = 1\,\mathrm{s}^{-1}$. Decreasing of moment of inertia increases the displacement, and amplifies the instability.

The original mechanical characteristics represent stable configuration and the torsional displacement is extremely small (see Figure 18). In that case, the values computed using ALE formulation coincide with the ones computed using injection/suction boundary conditions. Since we wanted to compare the behaviour of injection/suction boundary conditions to ALE formulation, we carried out several simulations decreasing the moment of inertia I_θ of the cross-section (to increase the amplitude of oscillations), and ω_θ (to get less stable profile). In the captions of Figures 19–23, the quantities differing from the original values are defined.

As it can be seen from the results presented in Figures 18–23, similar trends are predicted using injection/suction boundary conditions and ALE formulation. This is consistent with the same qualitative behaviour observed when analysing the response to forced movement (see Figure 14) by those two methods. The results from fluid–structure interaction simulations confirm the results related to the stability of the profile, coming out from the forced movement analysis.

5. CONCLUSIONS

We developed a framework for the analysis of fluid–structure interaction problems in civil engineering applications (e.g. bridge and viaduct cross-sections) based on injection/suction boundary conditions.

In the stability analysis of civil engineering constructions, it is usually necessary to carry out a large number of instationary computations for different parameter values, both in a case of a study based on imposed movement of the structure, or when we employ a simple dynamics model for the structure. The approach based on the injection/suction boundary conditions presents a considerable reduction in the computational cost with respect to the ALE formulation, and the results presented in this study show rather good agreement with the experiments and ALE formulation (the trends seem to be predicted very well). However, for vortex shedding flows our results show that the truncated formula for $U \cdot n$ in the injection/suction boundary conditions does not lead to satisfactory results, except in special situations (e.g. high frequencies of forced movement).

Finally, although here we have analysed mostly small amplitude movements, an important thing to remark is that in stability analysis, this already covers a range of significant interest for the detection of instabilities, giving another argument in favour of the use of injection/suction boundary conditions for these purposes.

Thus, the presented results suggest the potential usefulness of injection/suction boundary conditions in practical engineering computations, although more comprehensive studies are called for to precisely determine the limits of applicability.

REFERENCES

1. Washizu K, Ohya O, Otsuki Y, Fujii K. Aeroelastic instability of rectangular cylinders in a torsional mode due to a transverse wind. *Journal of Sound and Vibration* 1980; **724**:507–521.
2. Otsuki Y, Washizu K, Tomozawa H, Ohya O. A note on the aeroelastic instability of a prismatic bar with square section. *Journal of Sound and Vibration* 1974; **342**:233–248.
3. Washizu K, Ohya O, Otsuki Y, Fujii K. Aeroelastic instability of rectangular cylinders in a heaving mode. *Journal of Sound and Vibration* 1978; **592**:195–210.

4. Matsumoto M, Daito Y, Yoshizumi F, Ichikawa Y, Yabutani T. Torsional flutter of bluff bodies. *Journal of Wind Engineering and Industrial Aerodynamics* 1997; **69–71**:871–882.
5. Renou JY. Une méthode Eulerienne pour le calcul de forces fluide-élastique. *Thèse* de l'Université Paris VI, 1998.
6. Bardos C, Pironneau O. Petites perturbations et équations d'Euler pour l'aéroélasticité. *Modélisation Mathematique et Analyse Numérique* 1994; **28**(4):463–497.
7. Debiez C. Etude d'un traitement par petits perturbations du domaine pour l'équation d'Euler instationnaire. *INRIA*, *RR-2691*, 1995.
8. Lesoinne M, Fahrat C. Geometric conservation laws for aeroelastic computations using unstructured dynamic meshes. *AIAA Paper*, *95-1709*, 1995.
9. Nomura T, Hughes TJR. An arbitrary Lagrangian–Eulerian finite element method for interaction of fluid and a rigid body. *Computer Methods in Applied Mechanics and Engineering* 1992; **95**:115–138.
10. Donea J, Giuliani S, Halleux JP. An arbitrary Lagrangian–Eulerian finite element method for transient dynamic fluid–structure interactions. *Computer Methods in Applied Mechanics and Engineering* 1982; **33**:689–723.
11. Watanabe S, Hirano H, Kawahara M. A fluid–structure interaction analysis by ALE finite element method. *Proceedings of ECCOMAS 96*, Paris. Wiley: New York, 1996; 894–897.
12. Nkonga B, Guillard H. Godunov type method on non-structured meshes for three-dimensional moving boundary problems. *INRIA*, *RR-1883*, 1993.
13. Piperno S. Simulation numérique de phénomènes d'interaction fluide–structure. *Thèse* de l'École Nationale des Ponts et Chaussées, 1995.
14. Mittal S, Tezduyar TE. A finite element study of incompressible flows past oscillating cylinders and airfoils. *International Journal for Numerical Methods in Fluids* 1992; **15**:1073–1118.
15. Mittal S, Tezduyar TE. Parallel finite element simulation of 3D incompressible flows—fluid–structure interactions. *International Journal for Numerical Methods in Fluids* 1995; **21**:933–953.
16. Mohammadi B. An unified formulation for shape optimization and flow control. *International Journal for Numerical Methods in Fluids* 1998, submitted.
17. Stanciu M, Mohammadi B. Platform for multi-model design. *Flow*, *Turbulence and Combustion* 2000; **65**(3): 431–452.
18. Huffman WP, Melvin RG, Young DP, Johnson FT, Bussoletti JE, Bieterman MB, Hilmes CL. Practical design and optimization in computational fluid dynamics. *AIAA Paper*, *93-3111*, 1993.
19. Consortium Aerostructure. Dossier bibliographique des travaux de deux équipes de recherche (CAS Boulder et SINUS INRIA) liés au sujet du couplage fluide–structure. *INRIA*, *SINUS-CAS-98-1*, 1998.
20. Launder BE, Spalding DB. *Mathematical Models of Turbulence.* Academic Press: New York, 1972.
21. Mohammadi B, Pironneau O. *Analysis of the k–epsilon Turbulence Model*. Wiley: New York, 1994.
22. Begue C, Cardos B, Pares C, Pironneau O. Simulation of turbulence with a transient mean. *International Journal for Numerical Methods in Fluids* 1990; **11**:677–695.
23. Franke R, Rodi W. *Shear Flows*. Munich, Germany, 1991.
24. Iaccarino G, Ooi A, Durbin PA, Behnia M. Reynolds averaged simulation of unsteady separated flow. *International Journal of Heat and Fluid Flow*, 2002, to appear.
25. Durbin PA. A perspective on recent developments in RANS modeling. *The 5th International Symposium on Engineering Turbulence Modeling & Measurements*, Mallorca, Spain. 2002.
26. Medic G, Mohammadi B. *NSIKE*: *an incompressible Navier–Stokes solver for unstructured meshes.* INRIA, RR-3644, 1999.
27. Chorin JA. Numerical solution of the Navier–Stokes equations. *Mathematics of Computation* 1968; **22**: 745–762.
28. Gresho PM. On the theory of semi-implicit projection methods for viscous incompressible flows and its implementation via a finite element method. *International Journal for Numerical Methods in Fluids* 1990; **11**:587–620.
29. Struijs R, Deconinck H, de Palma P, Roe P, Powel GG. Progress on multidimensional upwind Euler solvers for unstructured grids. *AIAA Paper 91-1550*, 1991.
30. Medic G, Mohammadi B. A critical evaluation of the classical *k*-epsilon model and wall-laws for unsteady flows over bluff bodies. *International Journal for Computational Fluid Dynamics* 1998; **101**:1–12.
31. Medic G. Mathematical analysis of Reynolds stress turbulence models and numerical simulation of turbulent flows over fixed and moving boundaries. *Ph.D. Thesis*, Université Paris VI, Laboratoire d'Analyse Numérique.
32. Martin R. Développment de méthodes de calcul efficaces pour des écoulements instationnaires en géométrie déformable. *Thèse* de l'Université de Nice-Sophia Antipolis, 1996.
33. Marocco A. Simulations numeriques dans la fabrication des circuits à semiconducteurs (process modelling). *INRIA*, *RR-0305*, 1984.

